Electronic Supplementary Material (ESI) for EES Catalysis.

Supporting Information

Au-decorated Sb_2Se_3 photocathodes for solar-driven CO_2 reduction

John Mark Christian M. Dela Cruz, [a] Ádám Balog, [a] Péter S. Tóth, [a] Gábor Bencsik, [a] Gergely F. Samu [a,b] and Csaba Janáky * [a,b]

[a] Department of Physical Chemistry and Materials Science, Interdisciplinary Excellence Centre, University of Szeged, Aradi Square 1, Szeged, H-6720, Hungary

[b] ELI-ALPS, ELI-HU Non-Profit Ltd., Wolfgang Sandner street 3., Szeged, H-6728, Hungary

Figures

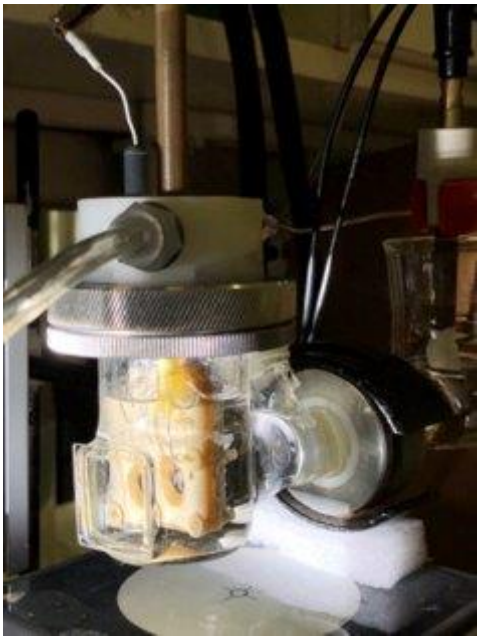

Figure S1. Photograph of the H-cell setup showing the cell holder made from PEEK. Exposed illuminated area is 0.28 cm^2 corresponding to a circular area with a diameter of 6 mm.

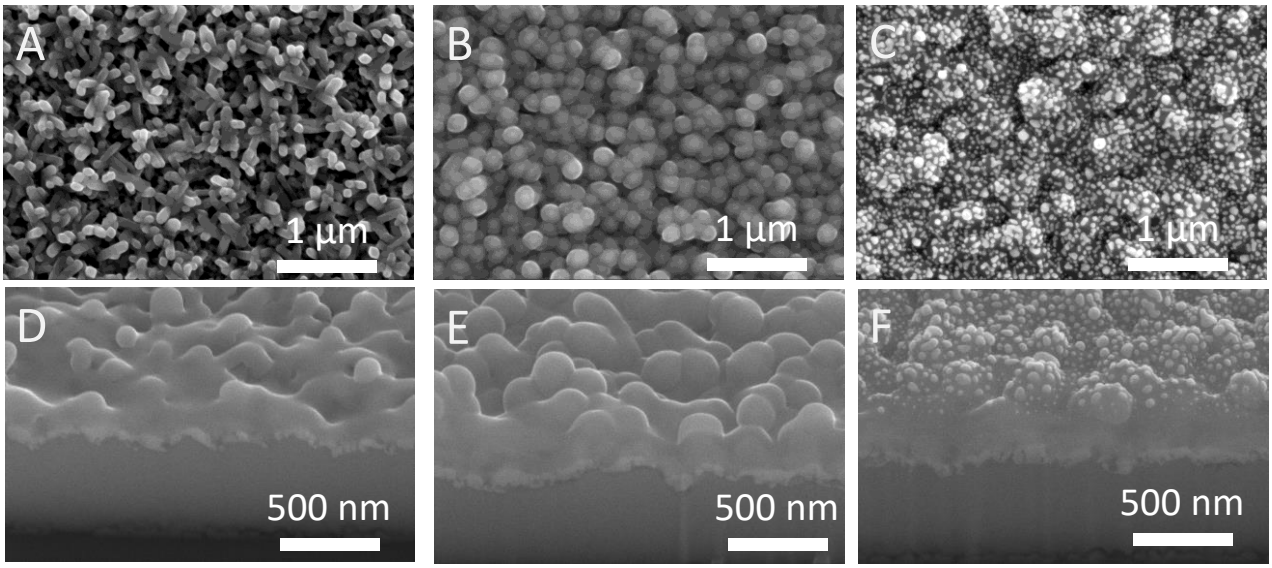

Figure S2. (A,B,C) Top-down and (D,E,F) Cross-section SEM images of (A,D) FTO/Au/Sb_2Se_3 , (B,E) FTO/Au/Sb_2Se_3/TiO_2 , and (C,F) FTO/Au/Sb_2Se_3/TiO_2/Au with 75 mC/cm2 of charge passed for Au deposition at −0.25 V vs Ag/AgCl.

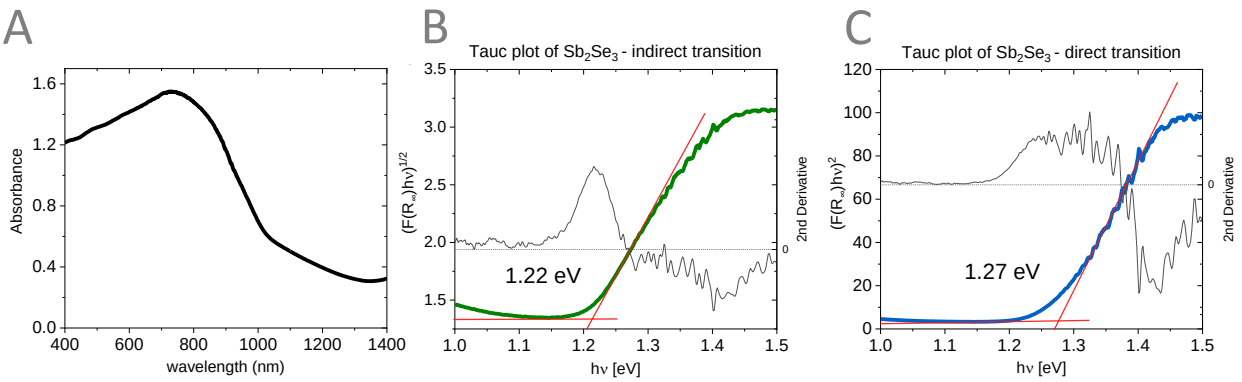

Figure S3. (A) UV Vis-NIR absorbance spectrum of the Sb_2Se_3 deposited on FTO with Tauc plots for band gap determination where (B) is for indirect transition analysis and (C) is for direct transition analysis. Sb_2Se_3 is reported to have very close indirect and direct transition.

Bandgap analysis: The bandgap analysis was done using the Tauc-plot method as seen in **Figure S3.** After measuring the diffused reflectance spectrum of Sb_2Se_3 deposited on FTO, the data was converted to the absorption spectrum using the Kubelka-Munk function.[1]

To determine the bandgap, we plotted the corresponding $(F(R_\infty)hv)^{1/\gamma}$ vs hv for both indirect and direct transitions, where γ is 2 for indirect transitions and ½ for direct transitions. The two types of transitions are known to exist for Sb_2Se_3.[2] These calculations led to the graphs in **Figure S3b** and **S3c**. On the resulting Tauc-plots, we determined the bandgap energy by linear fitting the steep region of the curves. To accurately determine the linear fit, the 2nd derivative method was used to find the inflection point on the curve. A tangent line on the inflection point of the curve was then drawn and extrapolated to the base to find the bandgap values.

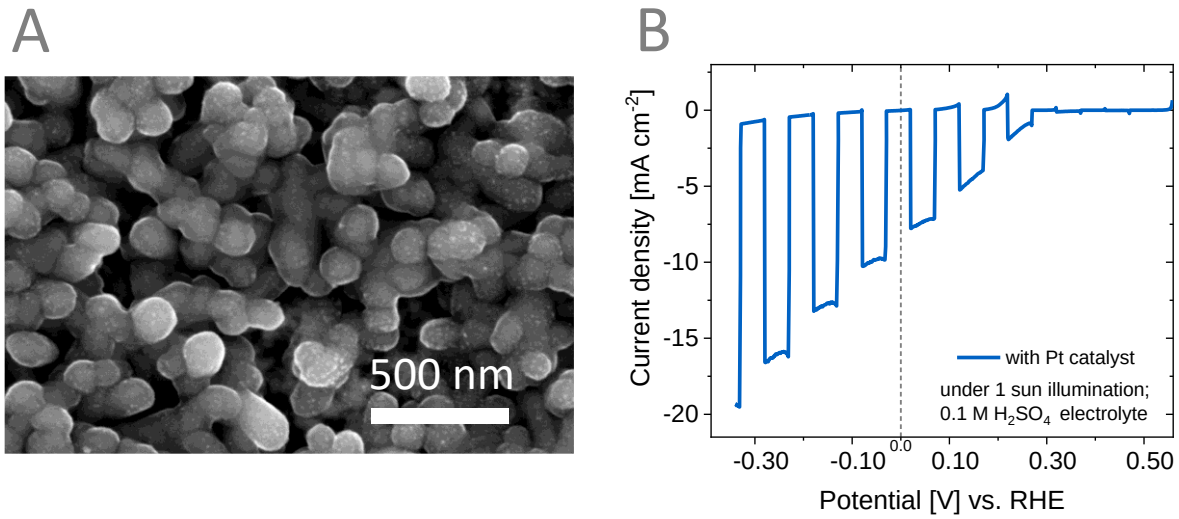

Figure S4. (A) SEM image of the photoelectrode with Pt cocatalyst. (B) Chopped light voltammogram of the photoelectrode with Pt catalyst for HER. Glassy carbon as counter electrode and Ag/AgCl as reference electrode.

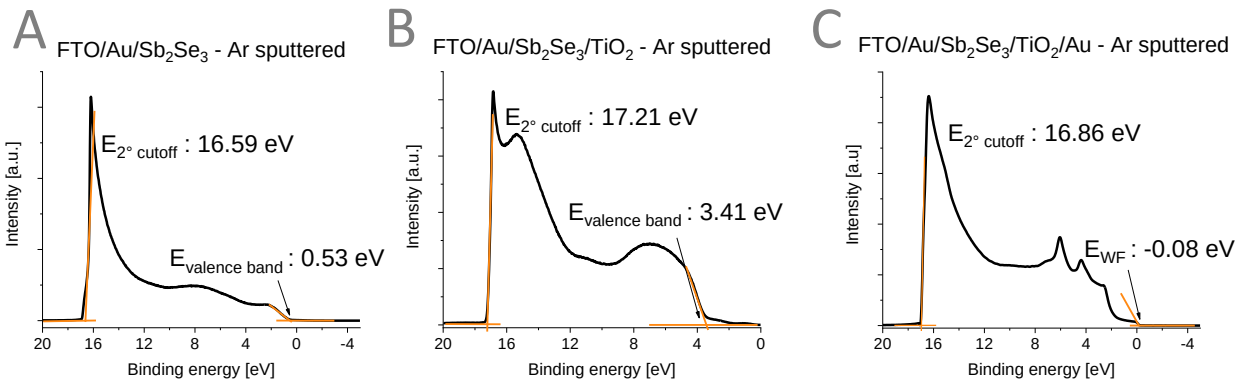

Figure S5. UPS spectra of the different assemblies, from (A) FTO/Au/Sb_2Se_3, to adding the TiO_2 layer (B), and up to adding the Au catalyst (C) showing the corresponding secondary electron cutoff energies and the valence band maxima/work function.

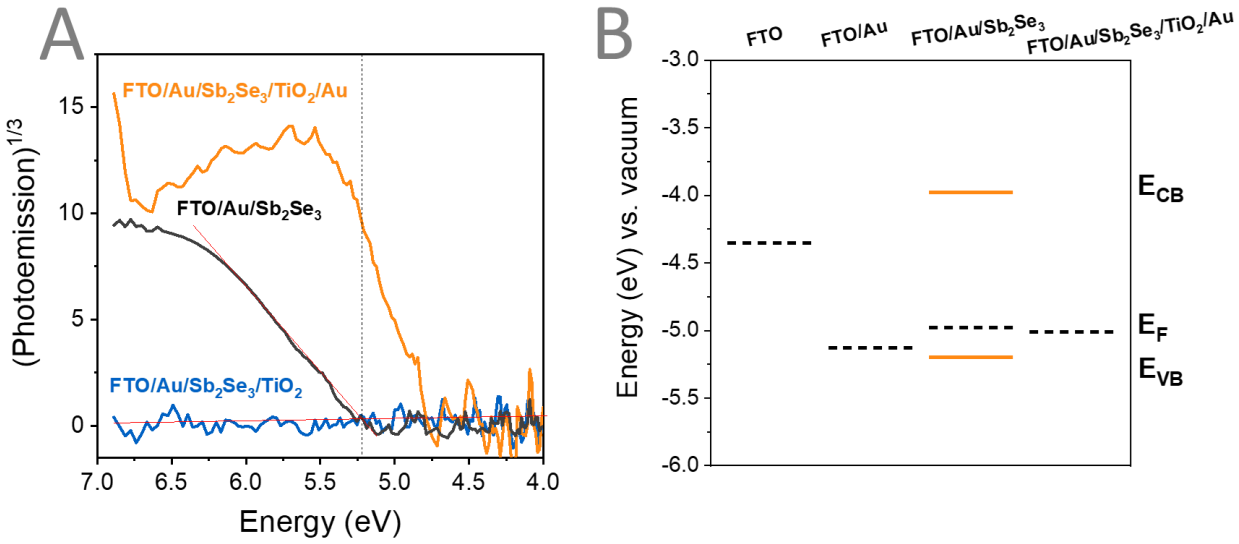

Figure S6. (A) Ambient Pressure Photoemission Spectra (APS) of the different assemblies. The APS curve of the FTO/Au/Sb_2Se_3 is used to determine the valence band position shown in (B). APS measurements were obtained at the range of 180nm-310nm. (B) Band diagram determined by contact potential difference, surface photovoltage spectroscopy, and ambient pressure photoemission spectroscopy measurements shown in Table S3. The valence band position of TiO_2 (E_{VB} = 7.4 eV) was outside the limit of the APS instrument (6.9 eV).

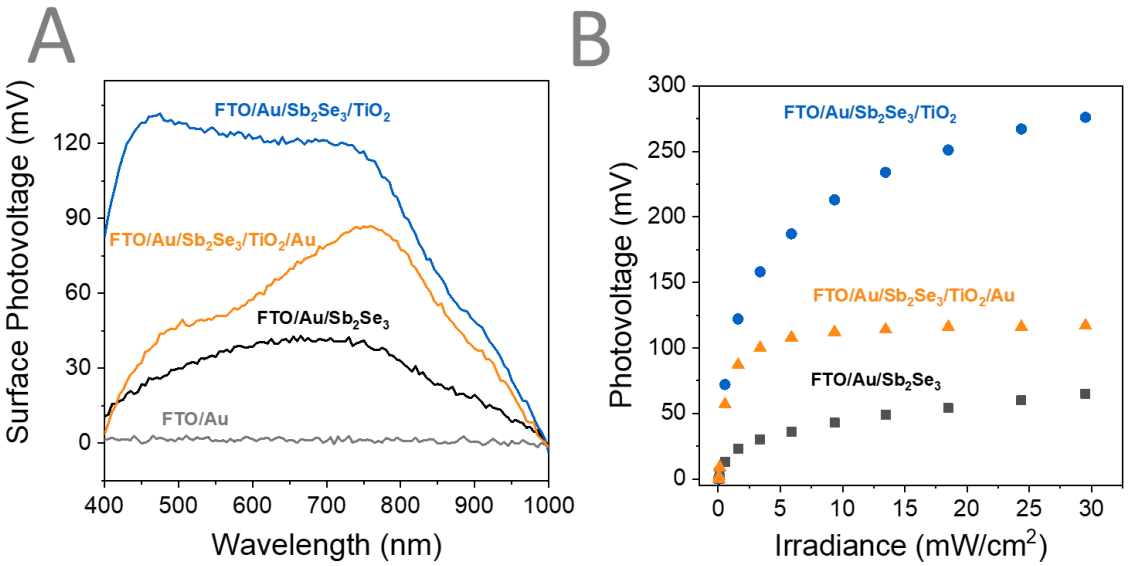

Figure S7. (A) Surface photovoltage spectra recorded in the wavelength range of 1000 nm – 400 nm and (B) Surface photovoltage measurements with white light illumination recorded for different intensities for the different photoelectrode assemblies.

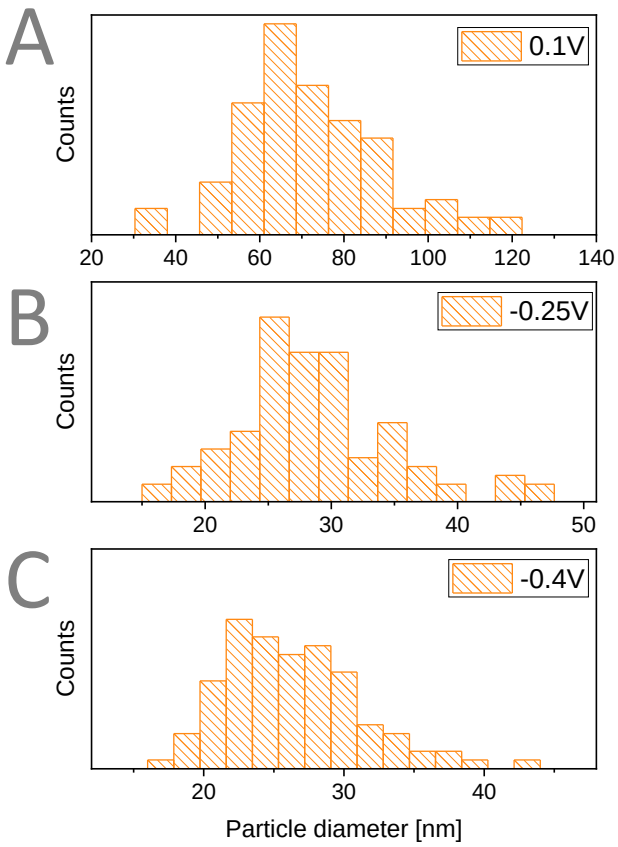

Figure S8. Size distribution of the Au nanoparticles for a total passed charge of 25 mC cm^{-2} deposited at (A) 0.1V, (B) -0.25V, and (C) -0.4V vs Ag/AgCl. Particle diameters are obtained through ImageJ processing.

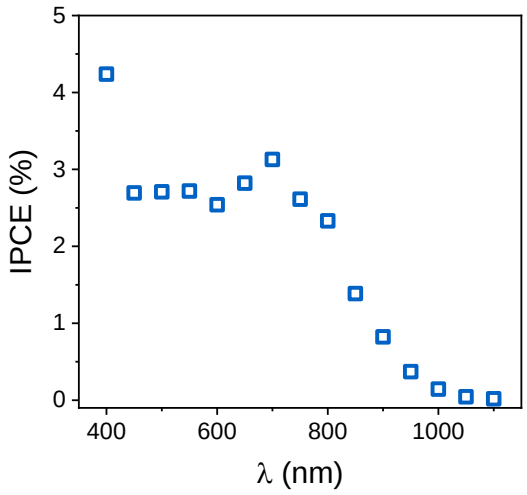

Figure S9. Incident-photon-to-current-efficiency (IPCE) curve of the FTO/Au/Sb_2Se_3/TiO_2/Au photoelectrode using potentiostatic measurement at −1.0 V vs. Ag/AgCl (− 0.37 V vs RHE).

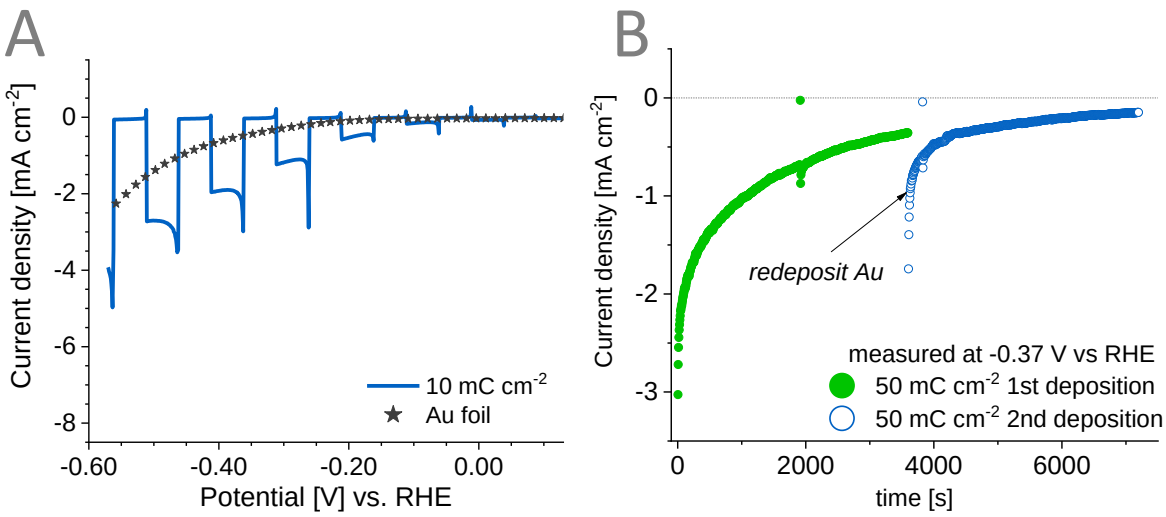

Figure S10. Performance of FTO/Au/Sb_2Se_3/TiO_2/Au photoelectrode with (A) lower amount of Au catalyst: 10 mC cm^{-2} deposited at −0.25V vs Ag/AgCl and (B) when the Au was redeposited after 1 hour of long-term measurement at −0.37V vs RHE. Initial amount was 50 mC cm^{-2} at −0.25V vs Ag/AgCl and redeposition was also performed with 50 mC cm^{-2} .

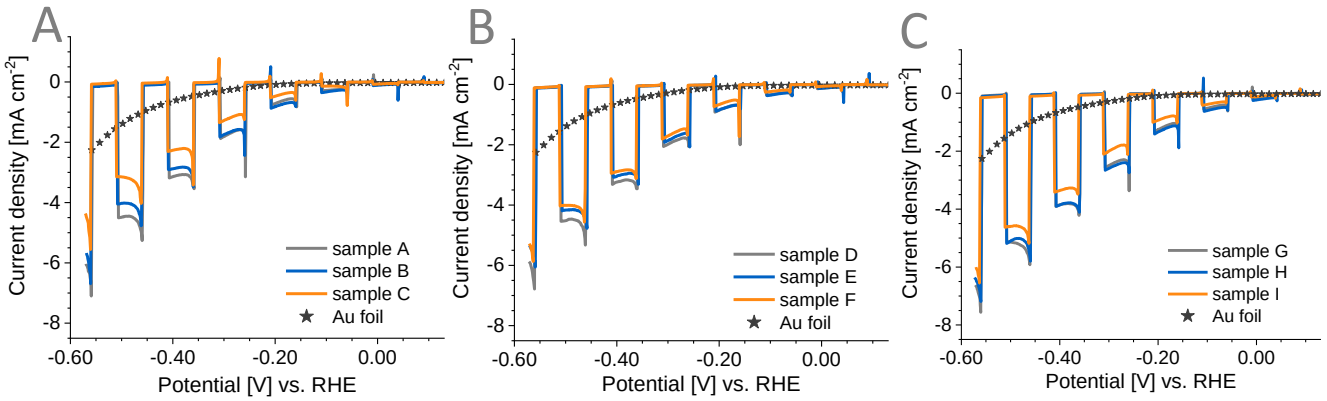

Figure S11. Performance of FTO/Au/Sb_2Se_3/TiO_2/Au photoelectrodes with different amount of Au catalyst: (A) 25 mC cm^{-2}, (B) 50 mC cm^{-2} and (C) 75 mC cm^{-2} deposited at an applied bias of −0.25V vs Ag/AgCl.

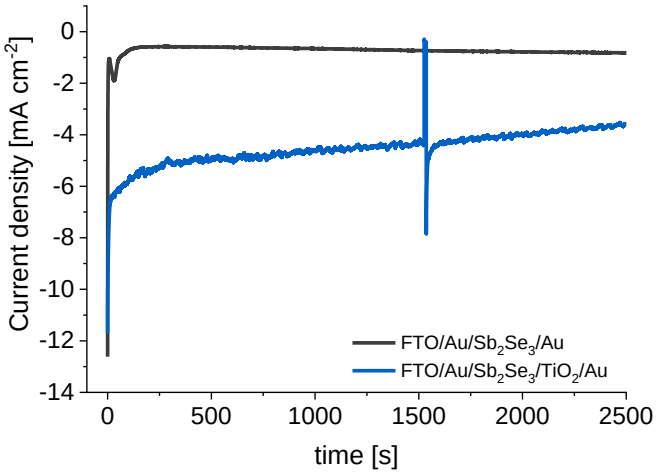

Figure S12. Chronoamperogram of the photoelectrode without the TiO_2 layer showing its poor performance. Both measured at −1.2 V vs Ag/AgCl (−0.57 V vs RHE) under 1 sun illumination (AM1.5G, 100 mW cm^{-2}) in CO_2-saturated solution of 0.5 M $KHCO_3$.

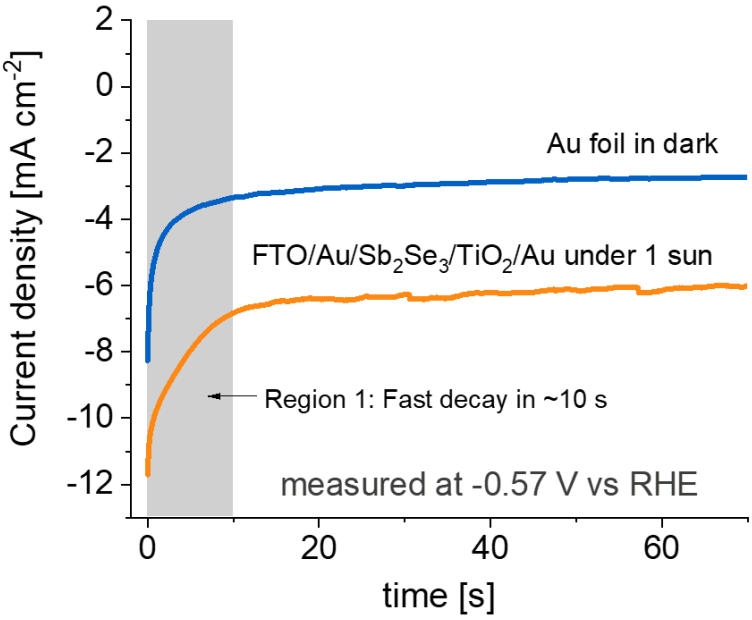

Figure S13. Chronoamperometry curve of a Au foil under similar conditions shows that the initial decay is inherent to Au. The same cell holder with the same exposed area was used for testing the Au foil and the photoelectrode. The electrolyte used is CO_2-saturated 0.5M $KHCO_3$ with continuous bubbling and stirring.

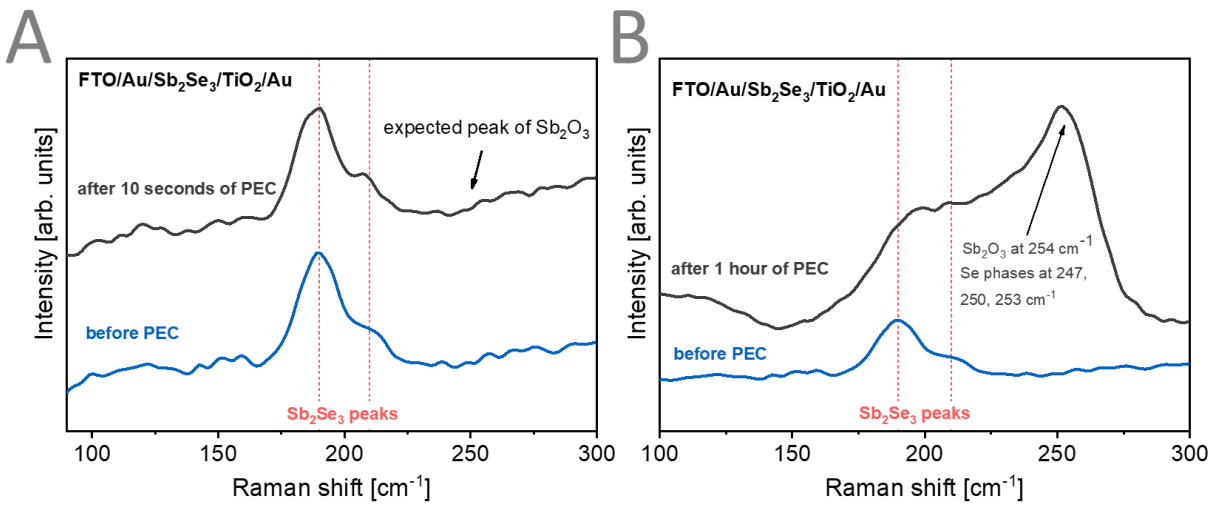

Figure S14. Post-PEC Raman spectra of the photoelectrode after (A) 10 seconds and (B) 1 hour of photoelectrolysis.

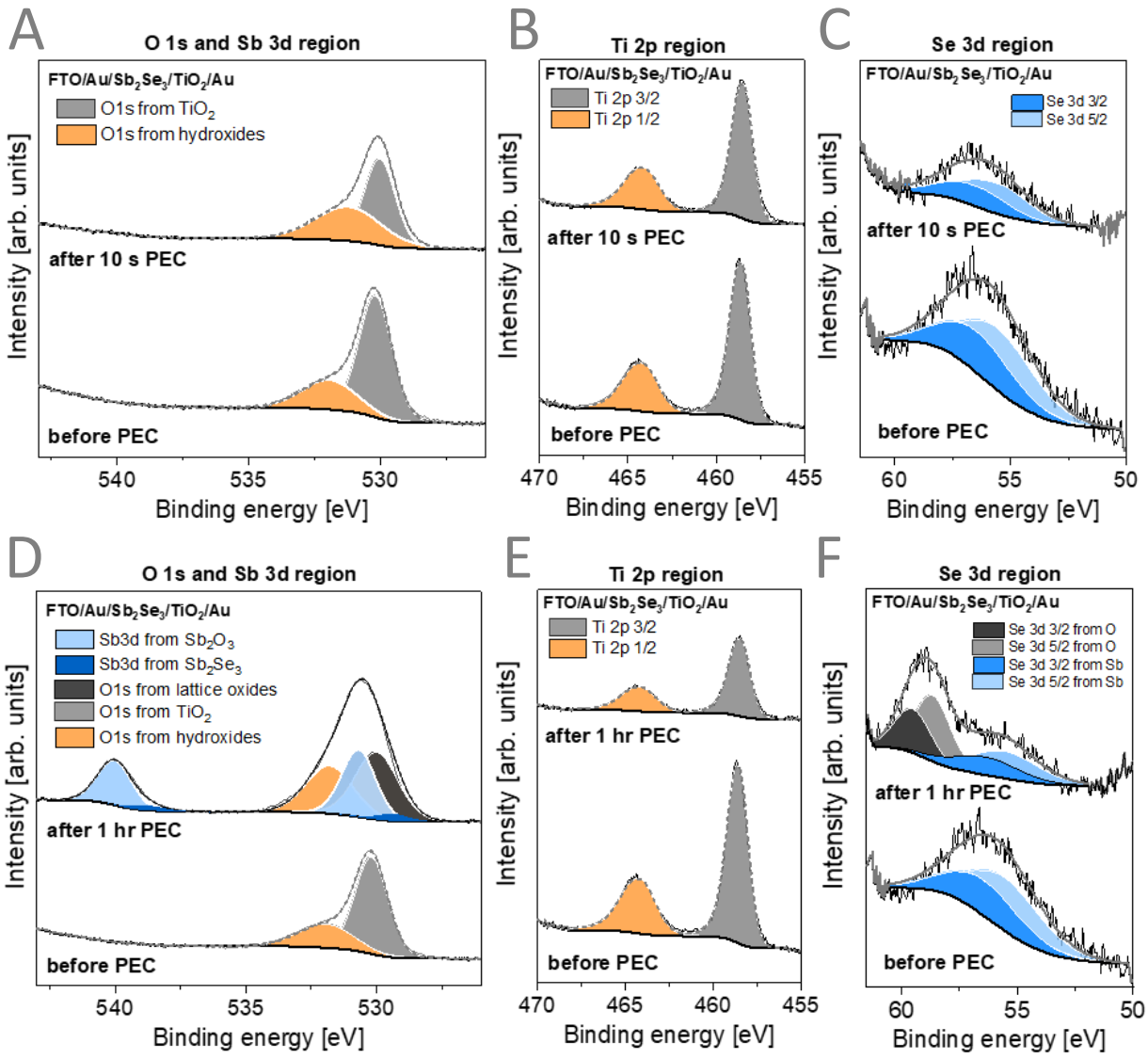

Figure S15. Post-PEC XPS spectra of the photoelectrode after 10 seconds (A, B, C) and 1 hour (D, E, F) of photoelectrolysis.

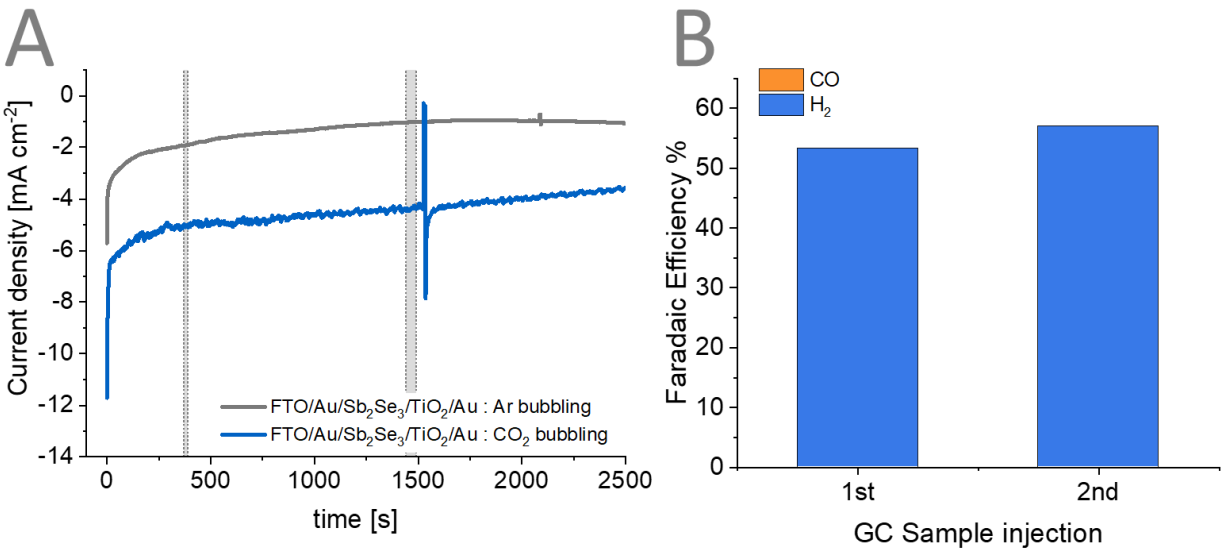

Figure S16. Chronoamperometry curve recorded using Ar bubbling vs CO_2 bubbling both measured at −0.57 V vs RHE. (B) Faradaic efficiency for the photoelectrolysis performed with Ar bubbling

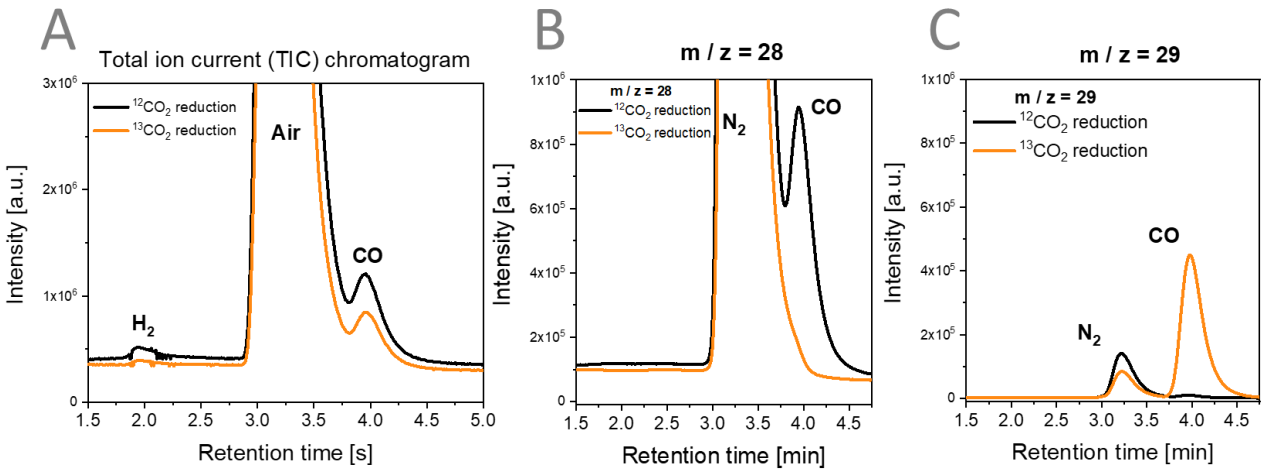

Figure S17. (A) Total ion current chromatogram and Selected-ion monitoring chromatograms at (B) m/z = 28 and at (C) m/z = 29 for the Isotope-labeled experiment wherein $^{13}CO_2$ and $KH^{13}CO_3$ were used to identify the source of the CO product.

Tables

Table S1. Raman spectroscopy shifts with corresponding symmetry of Sb_2Se_3 from literature.

	Symmetry	**Raman shift [cm^{-1}]**	**Reference**
Sb_2Se_3	A_{2g}	190	[3]
		191	[4]
		190	[5]
	A_{1g}	213	[3]
		211	[4]
		215	[5]
Sb_2O_3	A_g	253	[4]
		254	[5]
Se	A_{1g}	247	[5,6]
	E_u	253	[5,6]

Table S2. Binding energies for different species obtained experimentally versus data according to literature.

Species	**Experimental Binding energy [eV] pristine samples**	**Experimental Binding energy [eV] after 1 hr photo-electrolysis (from Figure S15)**	**Literature Binding energy [eV]** **with Reference**
(Sb_2Se_3) Sb 3d 5/2	529.17	529.37	530.4 [8] 529.65 (fresh) [9] 529.92 (etched) [9] 529.6 [10]
(Sb_2Se_3) Sb 3d 3/2	538.51	538.71	539.02 (fresh) [9] 538.87 (etched) [9] 538.9 [10]
Se 3d 5/2	53.61	58.62	54.23 [9] 55.0 [11] 54.3 [10]
Se 3d 3/2	54.47	59.48	55.07 [9] 55.8 [11] 55.1 [10]
(Sb_2O_3) Sb 3d 5/2	530.38	530.68	531.2 [8] 530.1 [12] 530 [13]
O 1s	532.56	-	533.7 [8] 532.91 [9]
Ti 2p 3/2	458.33	458.46	459.0 [14] 460 [15]

**Fresh* and *etched* differentiates samples that have been plasma-etched

Table S3. Band diagram values according to Contact Potential Difference, Surface Photovoltage Spectroscopy, and Ambient Pressure Photoemission Spectroscopy results. The values presented in italic are not included in the band diagram in **Figure S6B**.

SPECIMEN	E_{VB} (EV)	E_F (EV)	E_{CB} (EV)	E_G (EV)
FTO		-4.35 ± 0.05		
FTO/Au		-5.13 ± 0.03		
FTO/Au/Sb_2Se_3	-5.20 ± 0.02	-4.98 ± 0.02	-3.98	*1.22 **
FTO/Au/Sb_2Se_3/TiO_2		*-4.43 ± 0.02*		
FTO/Au/Sb_2Se_3/TiO_2/Au		-5.01 ± 0.03		

*data from **Figure S3**

Table S4. Summary of photoelectrode performances in CO2RR for CO production in aqueous electrolytes.

Assembly	Photocurrent density (mA cm^{-2})	Electrolyte	Illumination intensity (mW cm^{-2})	Faradaic efficiency for CO	Reference
FTO/Au/Sb_2Se_3/TiO_2/Au	**7.5 at –0.57 V_{RHE}**	**0.5 M $KHCO_3$**	**100**	**30% at –0.57 V_{RHE}**	**This work**
p-i-n a-Si/TiO_2/Au_{GB}	5 at –0.1 V_{RHE}	0.1 M $KHCO_3$	100	50% at –0.1 V_{RHE}	[12]
pn^+-Si/GaN_{NW}/Au	21 at –0.2 V_{RHE}	0.5 M $KHCO_3$	100	35% at +0.17 V_{RHE}	[13]
InP_{NW}/Au–TiO_2	5 at –0.1 V_{RHE}	0.1 M $KHCO_3$	100	84.2% at –0.1 V_{RHE}	[14]
ZnO/ZnTe/Au	16 at –0.7 V_{RHE}	0.5 M $KHCO_3$	100	63% at –0.5 V_{RHE}	[15]
pn^+-Si NW/Au_3Cu	7 at –0.5 V_{RHE}	0.1 M $KHCO_3$	33.33	80% at –0.2 V_{RHE}	[16]
pn^+-Si/Au	7.5 at –0.5 V_{RHE}	0.2 M $KHCO_3$	100	91% at –0.03 V_{RHE}	[17]
pn^+-Si/TiO_2/Au	8 at –0.8 V_{RHE}	0.1 M $KHCO_3$	100	86% at –0.8 V_{RHE}	[18]
Si/Au_{buried}	13.1 at –1.0 V_{RHE}	0.1 M $KHCO_3$	100	82.2% at –0.4 V_{RHE}	[19]

*NW subscript = nanowires, GB = grain boundaries

References

1 P. Makuła, M. Pacia and W. Macyk, *J. Phys. Chem. Lett.*, 2018, **9**, 6814–6817.
2 R. Vadapoo, S. Krishnan, H. Yilmaz and C. Marin, *Phys. Status Solidi B*, 2011, **248**, 700–705.
3 N. Fleck, T. D. C. Hobson, C. N. Savory, J. Buckeridge, T. D. Veal, M. R. Correia, D. O. Scanlon, K. Durose and F. Jäckel, *J. Mater. Chem. A*, 2020, **8**, 8337–8344.
4 W. Yang, S. Lee, H.-C. Kwon, J. Tan, H. Lee, J. Park, Y. Oh, H. Choi and J. Moon, *ACS Nano*, 2018, **12**, 11088–11097.
5 J. Tan, W. Yang, Y. Oh, H. Lee, J. Park, R. Boppella, J. Kim and J. Moon, *Adv. Energy Mater.*, 2019, **9**, 1900179.
6 Z. Sui, S. Hu, H. Chen, C. Gao, H. Su, A. Rahman, R. Dai, Z. Wang, X. Zheng and Z. Zhang, *J. Mater. Chem. C*, 2017, **5**, 5451–5457.
7 On the identification of Sb2Se3 using Raman scattering | MRS Communications | Cambridge Core, https://www.cambridge.org/core/journals/mrs-communications/article/on-the-identification-of-sb2se3-using-raman-scattering/7EE50C8F2212D8C4DA04A1DC2B870957, (accessed 4 December 2023).
8 M. B. Costa, F. W. S. Lucas, M. Medina and L. H. Mascaro, *ACS Appl. Energy Mater.*, 2020, **3**, 9799–9808.
9 X. Liu, J. Chen, M. Luo, M. Leng, Z. Xia, Y. Zhou, S. Qin, D.-J. Xue, L. Lv, H. Huang, D. Niu and J. Tang, *ACS Appl. Mater. Interfaces*, 2014, **6**, 10687–10695.
10 Y. Cheng, M. Gong, T. Xu, E. Liu, J. Fan, H. Miao and X. Hu, *ACS Appl. Mater. Interfaces*, 2022, **14**, 23785–23796.
11 H. Shiel, O. S. Hutter, L. J. Phillips, M. A. Turkestani, V. R. Dhanak, T. D. Veal, K. Durose and J. D. Major, *J. Phys. Energy*, 2019, **1**, 045001.
12 C. Powell, 1989.
13 J. Moulder, W. Stickle, W. Sobol and K. D. Bomben, 1992.
14 J. Saari, H. Ali-Löytty, M. M. Kauppinen, M. Hannula, R. Khan, K. Lahtonen, L. Palmolahti, A. Tukiainen, H. Grönbeck, N. V. Tkachenko and M. Valden, *J. Phys. Chem. C*, 2022, **126**, 4542–4554.
15 A. C. Bronneberg, C. Höhn and R. van de Krol, *J. Phys. Chem. C*, 2017, **121**, 5531–5538.